Horizon brightness revisited: measurements and a model of clear-sky radiances

Raymond L. Lee, Jr.

Clear daytime skies persistently display a subtle local maximum of radiance near the astronomical horizon. Spectroradiometry and digital image analysis confirm this maximum's reality, and they show that its angular width and elevation vary with solar elevation, azimuth relative to the Sun, and aerosol optical depth. Many existing models of atmospheric scattering do not generate this near-horizon radiance maximum, but a simple second-order scattering model does, and it reproduces many of the maximum's details.

Key words: Horizon brightness, clear-sky radiance, digital image analysis, atmospheric optics, multiple scattering.

Introduction

To the uninitiated, the clear daytime sky seems such a commonplace that its radiance and brightness[1] distribution surely must be well known. Researchers in fields ranging from solar energy engineering[2,3] to atmospheric optics[4,5] have repeatedly measured and modeled the angular distribution of clear-sky radiances, and they have published scores of papers on the subject. What can be left to know?

In fact, a great deal is left to know. In simple models of scattering by the clear atmosphere, radiance increases monotonically from the zenith to the astronomical (*i.e.*, dead-level) horizon.[6,7] However, a persistent feature of our cloudless atmosphere is a local maximum of radiance several degrees *above* the horizon, not *at* it. We have detected this near-horizon radiance maximum in clear daytime skies ranging from midlatitudes to the Antarctic, and from midcontinent to the open sea. However, no one, to my knowledge, has written about it. Why?

First, the maximum has rather low contrast, making it visually subtle. We tend to measure and model those sky features that call attention to themselves. Like many phenomena in atmospheric optics, the near-horizon maximum is obvious only to the initiated. Second, before the advent of narrow field-of-view (FOV) radiometers[8] and photographic analysis techniques,[9-12] accurate and detailed near-horizon radiance measurements were difficult, if not impossible, to make.

As a result, many previous models of clear-sky radiances have been compared with measurements that are fundamentally inadequate. This inadequacy stems from the measurements' limited angular resolution, which is often 5°–20°.[13-16] Obviously, any clear-sky features that are angularly smaller than this will either be eliminated or considerably smoothed. This imprecision in measurement has led, in turn, to models that fail to reproduce the near-horizon radiance maximum.[13-16] Authors of models that do produce a radiance maximum near the horizon have not commented on this feature, perhaps because they are unaware of its verisimilitude.[4,5,17]

Thus our goal here is threefold. First, we want to analyze clear-sky radiances near the horizon, using both spectroradiometry and digital image analysis. Second, we want to compare these radiance patterns with those predicted by a simple, but physically rigorous, solution of the radiative transfer equation to see if we can account for the near-horizon maximum. Finally, we want to see if our model provides us any insight into a simple physical explanation of the phenomenon.

High-Resolution Measurements of Clear-Sky Radiances

We begin by electronically digitizing, at a color resolution of 24 bits per pixel, color slides of clear skies seen at several sites and times of day (see Plates 37–40). Algorithms developed earlier[18] are used to calibrate the images colorimetrically and radiometrically. The digitized color slides yield relative radiance data

			Form Approved OMB No. 0704-0188

Report Documentation Page

Public reporting burden for the collection of information is estimated to average 1 hour per response, including the time for reviewing instructions, searching existing data sources, gathering and maintaining the data needed, and completing and reviewing the collection of information. Send comments regarding this burden estimate or any other aspect of this collection of information, including suggestions for reducing this burden, to Washington Headquarters Services, Directorate for Information Operations and Reports, 1215 Jefferson Davis Highway, Suite 1204, Arlington VA 22202-4302. Respondents should be aware that notwithstanding any other provision of law, no person shall be subject to a penalty for failing to comply with a collection of information if it does not display a currently valid OMB control number.

1. REPORT DATE **04 NOV 1993**	2. REPORT TYPE	3. DATES COVERED **00-00-1993 to 00-00-1993**

4. TITLE AND SUBTITLE **Horizon brightness revisited: measurements and a model of clear-sky radiances**	5a. CONTRACT NUMBER
	5b. GRANT NUMBER
	5c. PROGRAM ELEMENT NUMBER
6. AUTHOR(S)	5d. PROJECT NUMBER
	5e. TASK NUMBER
	5f. WORK UNIT NUMBER

7. PERFORMING ORGANIZATION NAME(S) AND ADDRESS(ES) **United States Naval Academy (USNA),Mathematics & Science Department,Annapolis,MD,21402**	8. PERFORMING ORGANIZATION REPORT NUMBER

9. SPONSORING/MONITORING AGENCY NAME(S) AND ADDRESS(ES)	10. SPONSOR/MONITOR'S ACRONYM(S)
	11. SPONSOR/MONITOR'S REPORT NUMBER(S)

12. DISTRIBUTION/AVAILABILITY STATEMENT
Approved for public release; distribution unlimited

13. SUPPLEMENTARY NOTES

14. ABSTRACT

15. SUBJECT TERMS

16. SECURITY CLASSIFICATION OF:			17. LIMITATION OF ABSTRACT	18. NUMBER OF PAGES	19a. NAME OF RESPONSIBLE PERSON
a. REPORT **unclassified**	b. ABSTRACT **unclassified**	c. THIS PAGE **unclassified**	**Same as Report (SAR)**	**9**	

whose angular resolution is limited only by the film; a resolution of $1/65°$ is possible. Relative sky radiances can then be extracted from the image data and displayed as meridional radiance profiles (*i.e.*, plots of normalized, azimuthally averaged radiance versus angular elevation). Figure 1 illustrates the major features of a surface-based observer's clear-sky scattering geometry.

At one site, color slides were taken simultaneously with narrow FOV spectra[19] of the clear sky (see Plate 37). Comparisons of these two data sources give a good indication of the photographic technique's potential accuracy (see Fig. 2). For elevation angles $\geq 0.5°$ in Fig. 2, the root-mean-square (rms) difference between the two normalized meridional profiles is 0.00802. The radiometer's maximum radiance occurs 1.5° above the astronomical horizon, whereas the photographic analysis places it at $\sim 2.4°$. Depending on solar elevation, azimuth relative to the Sun, and normal optical depth, the maximum may occur at 8° (or higher) and be much broader than that seen in Fig. 2. The breadth of the maximum and the close agreement of the photographic and the radiometer data suggest that we are not seeing the photographic equivalent of a Mach band (a possibility explored by Lynch[20]).

Nevertheless, the photographic and the radiometer data's disagreement about the maximum's elevation illustrates some of the inherent differences between the two techniques. First, the radiometer data were acquired over a period of ~ 25 min, meaning that they may incorporate temporal changes in sky radiance patterns that the photograph does not. Second, although the photographic data have been smoothed over a 0.5° azimuthal FOV, this digital smoothing may be somewhat different from that occurring optically in the radiometer. (The error bars of Fig. 3 illustrate the radiometric noise typical at this narrow FOV for the photographic technique.) Finally, we
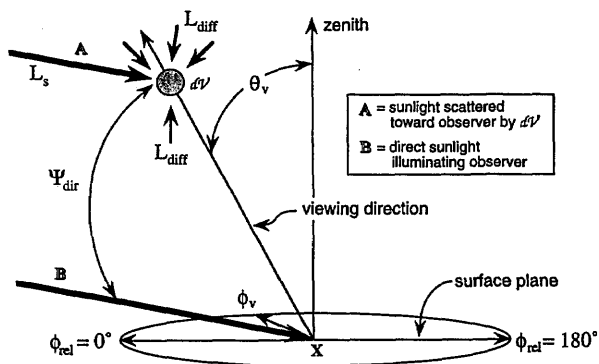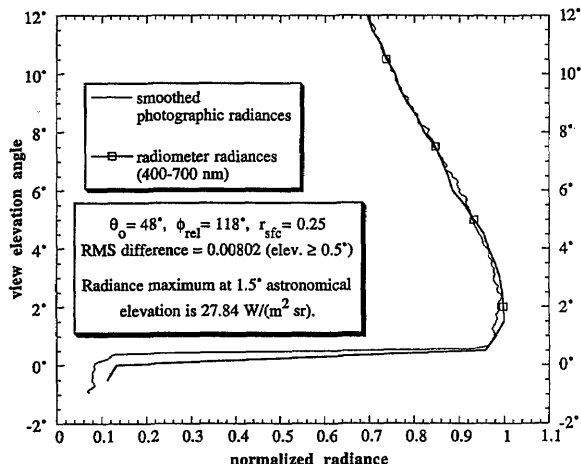

Fig. 2. Comparison of photographic and spectroradiometric measures of clear-sky radiances at University Park, Pa., at 1605 GMT on 6 October 1992 (see Plate 37). A running average has smoothed the detailed photographic data of Fig. 3. The solar zenith angle $\theta_0 = 48°$, the instruments' azimuth with respect to the sun, ϕ_{rel}, is 118°, and the equivalent Lambertian surface reflectance $r_{sfc} = 0.25$.

must correct the photographic analysis for any exposure falloff or vignetting that occurs in the camera.

Our Fig. 2 comparison of photographic and radiometer data suggests that, with careful geometric and radiometric calibration of photographic data, we can use digital image analysis when a radiometer is unavailable. When we do so, the resulting photographic radiance profiles confirm that the near-horizon maximum is a remarkably persistent feature of the clear daytime sky. How can we explain it?

Fig. 1. Clear-sky scattering geometry for an observer at point X whose view zenith and azimuth angles are θ_v and ϕ_v, respectively. ϕ_{rel} is the difference between the sun's azimuth and ϕ_v. Clear-sky radiances reaching the observer include contributions from directly scattered sunlight, L_s, and from multiply scattered surface light and skylight, L_{diff}. At each elemental scattering volume dV along the observer's line of sight, L_s and L_{diff} are scattered through various angles Ψ (Ψ_{dir} for L_s is shown above).
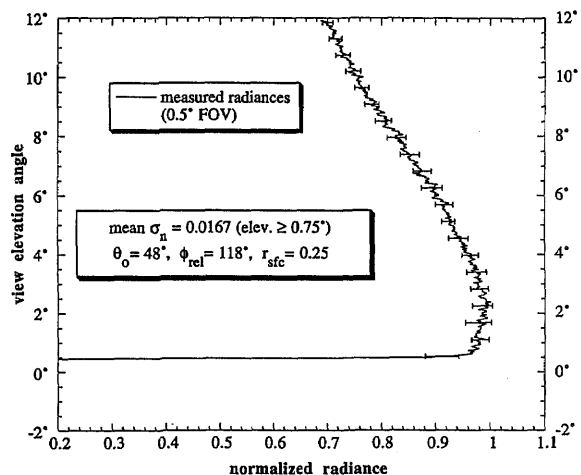

Fig. 3. Normalized radiance versus view elevation angle for a clear-sky scene at University Park, Pa., at 1605 GMT on 6 October 1992 (see Plate 37). The astronomical horizon corresponds to a view elevation of 0°. These photographically derived data span a 0.5°-wide meridional swath near the scene's center that matches the FOV of spectroradiometer data taken simultaneously (see Fig. 2). Error bars span two standard deviations σ_n of the azimuthal radiances at selected elevation angles.

Second-Order Scattering Model
for Clear-Sky Radiances

As noted above, models of clear-sky radiances are not in short supply.[2-5] Indeed, scores of models are available, ranging from the purely empirical to the highly theoretical. Although we can easily reject models that fail to produce the near-horizon maximum, why not use those that do?[4-5]

Aside from the difficulty of successfully translating others' algorithms, their authors themselves raise some cautions. Dave[17] says of his spherical harmonics model that "because of the plane-parallel [atmosphere] assumption and nature of the method of computations, it is not possible to evaluate" sky radiance at the astronomical horizon. Furthermore, he describes his algorithm as "somewhat unreliable" at 1° elevation, which is within the range where radiance maxima can occur. Prasad et al.[4] use their model (which incorporates van de Hulst's doubling method) to plot horizon-to-zenith profiles of sky radiance for several azimuth angles (see their Fig. 8). Surprisingly, their profiles do not appear to converge at the zenith where, at a particular time and for a particular atmosphere, only a single radiance is possible. Thus, despite the fact that these two models incorporate higher-order multiple scattering, both exhibit some shortcomings that are relevant to our problem. Given these shortcomings, developing a new model of sky radiance does not seem superfluous.

We start by applying the equation of radiative transfer to a curved-shell atmosphere in which scatterer number density decreases exponentially with altitude. Scatterers consist of molecules and spherical haze droplets, and slant optical paths are calculated by the use of Bohren and Fraser's algorithm.[21] The scattering model accounts for variations in solar elevation, scatterer optical depth, scale height, phase function, and Lambertian surface reflectance. It produces clear-sky radiances for a surface-based observer as a function of view zenith angle θ_v and view azimuth ϕ_v.

In the model, θ is the zenith angle, with $\theta = \pi$ being the nadir and $\theta = 0$ the zenith. ϕ is azimuth angle, and ϕ_{rel} is the relative azimuth ($\phi_{rel} = 0$ is toward the Sun, $\phi_{rel} = \pi$ is in the antisolar direction; see Fig. 1). $\Psi(\theta, \phi)$ is the scattering angle measured in spherical coordinates θ, ϕ. For scattering of direct sunlight, Ψ_{dir} is defined by the Sun, a scatterer (aerosol or molecule), and the observer. Atmospheric absorption is parameterized by the single-scattering albedo ϖ_0. For an observer at the Earth's surface, the diffuse clear-sky radiance L_{sky} in the direction θ_v, ϕ_v is

$$L_{sky} = \int_{\tau=0}^{\tau_f} J(\Psi, \tau) \exp(\tau - \tau_f) d\tau, \quad (1)$$

where the source function $J(\Psi, \tau) = J_{dir} + \Sigma_{i=1}^{\infty} J_{diff,i}$ is the sum of direct single scattering J_{dir} and all higher orders of diffuse multiple scattering $\Sigma_{i=1}^{\infty} J_{diff,i}$ along the total atmospheric slant optical path τ_f

coinciding with the observer's viewing direction. J_{dir} and $J_{diff,1}$ can easily be expanded as integrals over τ, θ, and ϕ, and the integrals can then be evaluated numerically. For realistic clear atmospheres, we show that for $\Psi_{dir} > 20°$ the multiple-scattering contributions to J_{diff} after the first term $J_{diff,1}$ do not affect L_{sky} profiles appreciably. In other words, we restrict our model to single plus double scattering, making it a second-order scattering model.

Assuming the solar radiance L_s is nearly constant over the Sun's small solid angle ω_s,

$$J_{dir} \approx \varpi_0 \exp(-\tau) \frac{\overline{L_s} \omega_s P_{dir}(\Psi)}{4\pi} = \varpi_0 E_s \exp(-\tau) \frac{P_{dir}(\Psi)}{4\pi},$$

$$(2)$$

where E_s is the Earth's solar constant ($= \overline{L_s}\omega_s$), $P_{dir}(\Psi)$ is the scattering phase function for direct scattering of sunlight, and τ is the integration variable in Eq. (1).

For diffuse multiple scattering, $J_{diff,1} = (\varpi_0/4\pi)$ $\int_{4\pi} P_{diff}(\Psi) L_{diff}(\Psi) d\omega$, or

$$J_{diff,1} = \frac{\varpi_0}{4\pi} \int_{\phi=0}^{2\pi} \int_{\theta=0}^{\pi} P_{diff}(\theta, \phi) L_{diff}(\theta, \phi) \sin(\theta) d\theta d\phi,$$

$$(3)$$

where P_{diff} is the scattering phase function for scattering of surface light and skylight from θ, ϕ into a differential air volume dV that lies along an observer's line of sight in the direction θ_v, ϕ_v. In general, the angles $\Psi(\theta, \phi)$ for scattering surface light and skylight into dV will not be the same as the observer's Ψ_{dir} as he or she looks toward dV.

The diffuse radiances $L_{diff}(\theta, \phi)$ that illuminate each dV are calculated by integrating over τ_{diff}, where τ_{diff} is the slant-path optical depth from dV to the top (or bottom, depending on θ) of the atmosphere in the direction θ, ϕ. Specifically,

$$L_{diff}(\theta, \phi) = L_{\uparrow sfc} \exp(-\tau_{\uparrow sfc})$$

$$+ \frac{\varpi_0}{4\pi} \int_0^{\tau_{diff}} E_s \exp(-\tau_{\theta\phi}) P_{\theta\phi} \exp(\tau - \tau_{diff}) d\tau.$$

$$(4)$$

In Eq. (4), $L_{\uparrow sfc}$ is the radiance reflected upward from the surface toward dV. $L_{\uparrow sfc}$ is attenuated exponentially along the slant optical path $\tau_{\uparrow sfc}$ between the Earth's surface and dV. Most of dV's θ, ϕ directions do not intersect the Earth's surface, so $L_{\uparrow sfc} = 0$ for them.

We assume that the surface behaves as a Lambertian reflector with reflectance r_{sfc}, making $L_{\uparrow sfc} = E_s$ $\cos(\theta_0)\exp(-\tau_{\downarrow sfc})r_{sfc}/\pi$. $\tau_{\downarrow sfc}$ is the slant optical path of direct sunlight (at zenith angle θ_0, azimuth ϕ_0) down to the surface, and is itself a function of θ, ϕ.

$E_s \cos(\theta_0)$ is the fraction of the solar irradiance that is projected normally onto the Lambertian surface.

Returning to Eq. (4), the $\tau_{\theta\phi}$ are the slant optical paths defined by the direction of the sun (θ_0, ϕ_0) and points *along* the direction θ, ϕ from dV. Physically, $\exp(-\tau_{\theta\phi})$ describes direct sunlight's attenuation between the top of the atmosphere and those points along τ as we move toward dV. The phase function $P_{\theta\phi}$ describes the scattering efficiency of direct sunlight toward dV from the direction θ, ϕ. Note that all the scattering phase functions $P(\Psi)$ used here are $f(\tau)$ because the ratio of aerosol to molecular scattering changes along the slant τ (the ratio changes because altitude changes along the slant paths).

In addition, two different aerosol phase functions are used, and these are based on Mie scattering calculations over two polydispersions, the Deirmendjian haze-L and haze-M size spectra.[22] Because we assume that the incident solar radiance L_s is unpolarized, the intensity distribution function for aerosol scattering (at the single-scattering level) is given by Ref. 22's Eq. (5-9). Our molecular-scattering phase function follows the Rayleigh-scattering criterion described in Eq. (4-37) of Ref. 22. When $\Psi_{dir} = 90°$, both multiple scattering and our aerosol size spectra will considerably reduce skylight's linear polarization from its theoretical upper limit of 100% (see, for example, McCartney's discussion[22] on pp. 195–196 and 231–233).

Performance of the Second-Order Model

For a wide range of parameters, the second-order scattering model does in fact generate a near-horizon radiance maximum. The model's maxima change both in angular breadth and elevation with changes in solar elevation, normal optical depth, and relative azimuth. Bear in mind that this simple model will not reproduce all the features found in more detailed models, such as those by Prasad *et al.*[4] and Dave.[17] However, near the horizon and at large scattering angles from the sun, the second-order model is often more realistic.[23] Thus, for our purposes, its strengths outweigh its weaknesses. We consider some specific cases.

Unlike Prasad *et al.*'s model, the second-order model produces azimuth-independent values of the zenith radiance, as shown in Fig. 4. As far as is possible in Fig. 4, we have matched model parameters with those used in Prasad *et al.*'s Fig. 8. Note also that, for this solar elevation and aerosol optical depth, the second-order model predicts that, at view elevations of $<20°$, the clear sky will be *brighter* in the backward direction ($\phi_{rel} = 180°$) than at right angles to the Sun's azimuth ($\phi_{rel} = 90°$). Although Dave's model behaves similarly near the horizon (see his model's behavior in Prasad *et al.*'s Fig. 8), Prasad *et al.* predict just the opposite. Which claim is more realistic?

Although no single set of measurements can be conclusive, Fig. 5 seems to support the second-order model's claims about the azimuthal behavior of clear-
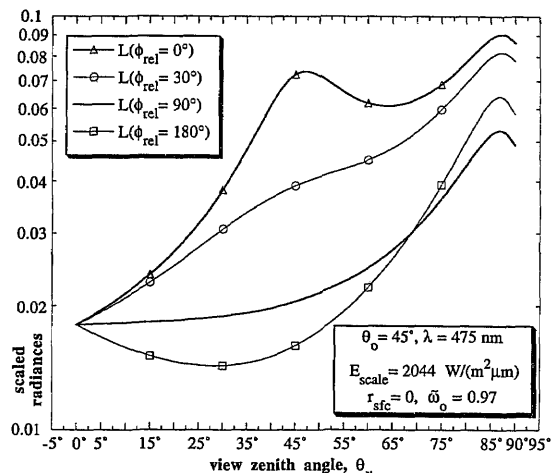

Fig. 4. Second-order scattering model's meridional radiance profiles for a combined molecular and aerosol atmosphere. Model parameters were chosen to closely match those of Fig. 8 in Ref. 4. Multiplying the scaled radiances [which include a factor of $1/(\pi$ sr)] by the solar spectral irradiance E_{scale} at wavelength λ converts them into absolute radiances.

sky radiances near the horizon. In Fig. 5, we see how relative radiances vary azimuthally across Plate 38, averaged over view elevation angles of 1°–20°. Now, using the same second-order model parameters that produce the best fit to the measured meridional radiance profile, we compare the azimuthal measurements with the model's behavior. The agreement between measurements and the model is quite good over the range $\phi_{rel} = 90°$–122° (the curves' rms difference is 0.0011). We do not know if the trend of L_{sky} increasing with ϕ_{rel} continues, but at least we know that $L(\phi_{rel})$ does not *decrease* monotonically beyond $\phi_{rel} = 90°$. As we look toward higher ϕ_{rel} near the horizon in Plate 38, we are approaching the
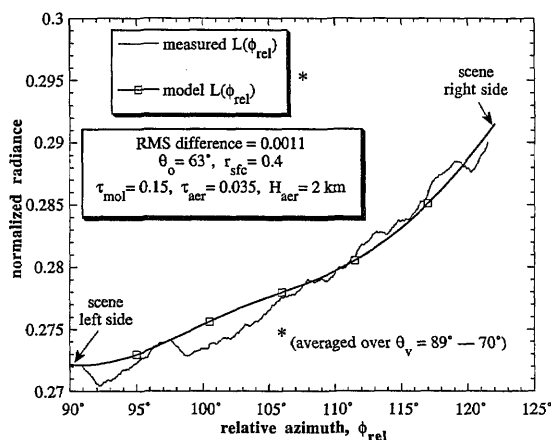

Fig. 5. Comparison of the azimuthal variation of clear-sky radiances across Plate 38 with those predicted by the second-order model, with the same model parameters that generate the best-fit meridional radiance profile of Fig. 6. τ_{mol} is the molecular normal optical depth, τ_{aer} is the aerosol normal optical depth, and H_{aer} is the aerosol scale height. A constant molecular scale height of 8.4 km and a single-scattering albedo ϖ_0 of 0.97 are used throughout this paper.

aerosol backscattering maximum. Thus both nature and simple physical reasoning suggest that the second-order model is correct in saying that, near the horizon, $L(\phi_{rel} = 180°) > L(\phi_{rel} = 90°)$.

The second-order model also produces the solar aureole, as evidenced by the local maximum near $\theta_v = 45°$ in Fig. 4's $L(\phi_{rel} = 0°)$ curve. However, compared with aureoles produced by Prasad et al.'s and Dave's models, the second-order model appears consistently to underestimate the aureole's magnitude. These underestimates are not surprising because we have considered only two scatterings and thus have disallowed higher-order scatterings into directions near the direct beam. In an atmosphere with a pronounced forward-scattering peak, we can expect this assumption to produce errors.

However, for $\Psi_{dir} \geq 20°$, the radiances of the three models are nearly equal. For example, at the zenith ($\Psi_{dir} = 45°$ for $\theta_0 = 45°$), the second-order model yields a radiance that is $\sim 23\%$ larger than that predicted by Dave's[17] model (see his Fig. 12) and $\sim 6\%$ smaller than the average zenith radiance in Prasad et al.'s[4] Fig. 8. At $\theta_v = 80°$ and $\phi_{rel} = 30°$ ($\Psi_{dir} = 43.5°$), the second-order model differs from the other two models by $\sim 9\%$, with the signs of the differences being the same as at the zenith (all comparisons have been corrected for spectral variations in E_s). These and other comparisons of the models are the basis for my above statement that we can usually ignore higher-order scattering contributions to L_{sky} profiles if we look at comparatively large scattering angles Ψ_{dir} from the Sun.

Comparisons of Measured and Modeled Radiance Profiles

When we compare our measured radiance profiles with those of the model, the agreement is usually quite good. By careful (and realistic) choice of model parameters, we can reduce the rms difference between the measured and the modeled radiance profiles to <0.04 for radiance profiles normalized by their respective maxima.

In Figs. 6–10 we have plotted the measured meridional radiance profiles of Plates 37–40 and of Plate 41 in Ref. 24. With the exception of Fig. 10, each profile is an azimuthal average across the entire scene (in Fig. 10, the simulated azimuthal FOV is 0.5°), and a typical standard deviation for these azimuthal radiance averages is 0.02. All view elevation and zenith angles are measured with respect to the astronomical horizon. The rms differences between modeled and measured radiances are limited to astronomical elevation angles above 0.25°–0.75° in order to reduce the highly variable contributions of surface reflectance (in Figs. 6 and 10, local topography rises $\sim 0.5°$ above the astronomical horizon).

Paired with each measured radiance profile is a best-fit profile from the second-order model. Our best-fit criterion attempts to minimize rms differences between the modeled and the measured profiles while simultaneously requiring the model's maxima
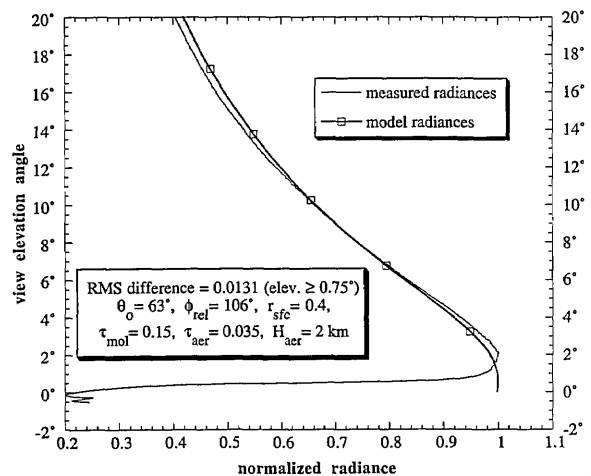

Fig. 6. Comparison of measured and modeled clear-sky radiances for the Bald Eagle Mountain scene at University Park, Pa., ~ 1530 GMT on 5 February 1987 (see Plate 38).

to occur within $\sim 1°$ of the observations' maxima. The parameters θ_0 (solar zenith angle), ϕ_{rel} (mean relative azimuth in the scene), and r_{sfc} (Lambertian surface reflectance) either are known or can be measured from the digitized images. Because τ_{mol} (molecular normal optical depth) and ϖ_0 (single-scattering albedo) are taken to be the constants 0.15 and 0.97, respectively, the variable parameters are the aerosol normal optical depth τ_{aer} and the aerosol scale height H_{aer}. Our best-fit values for these two parameters are quite plausible (see, for example, pp. 224–225 of Ref. 21 and Fig. 3 of Ref. 25).

The best fit occurs in Fig. 10 (rms difference 0.00378), and the poorest fit is seen in Fig. 9 (rms difference 0.035). The model's performance in Fig. 10 is especially reassuring because here we have the most detailed time, elevation, and azimuth data (see Plate 37). These details mean that θ_0 and ϕ_{rel} are known quite accurately, thus reducing uncertainties in the fitting algorithm.
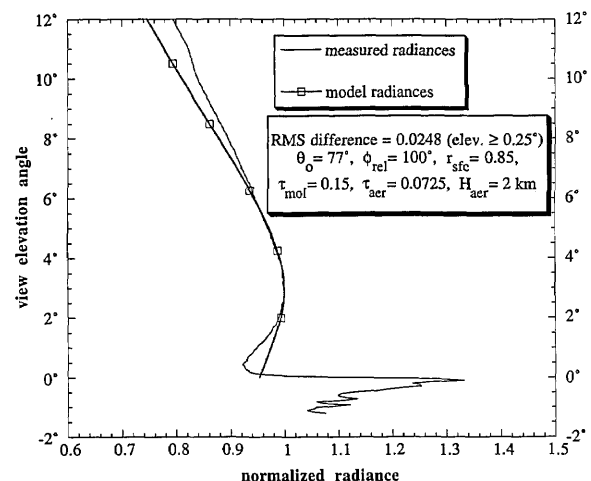

Fig. 7. Comparison of measured and modeled radiances for an Antarctic clear-sky scene (see Plate 39). Although the snow is brighter than the sky, radiances are still normalized here by a local maximum occurring above the horizon.
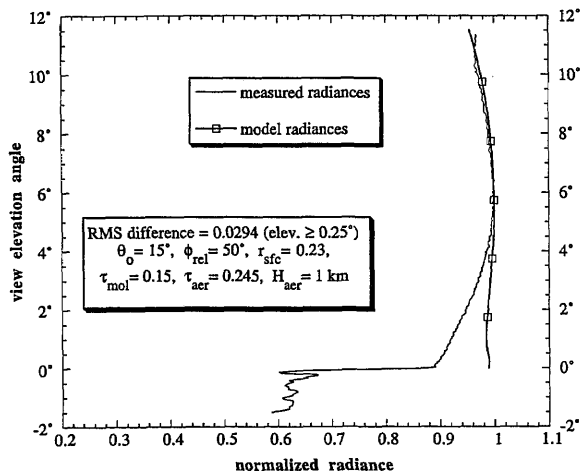
Fig. 8. Comparison of measured and modeled radiances for a clear-sky scene off Hamilton, Bermuda, at ~1530 GMT on 2 June 1988 (see Plate 40).

Fig. 10. Comparison of measured and modeled radiances for a clear-sky scene at University Park, Pa., at 1605 GMT on 6 October 1992 (see Plate 37).

In Fig. 9 we know θ_0 and ϕ_{rel} with nearly the same accuracy that we did in Fig. 10, yet Fig. 9 has the largest rms difference of the five scenes analyzed. Here the measurements and the model disagree chiefly near the horizon. The same error pattern occurs in Figs. 6 and 8, implying that the second-order model's parameterizing of surface contributions to L_{sky} is the source of the problem. Nevertheless, the model *does* accurately reproduce the position and general features of the near-horizon maximum. Because Prasad *et al.*'s and Dave's models also use Lambertian lower boundaries, they may have no better success in accurately describing the sky radiance distributions seen above real topography.

What general conclusions can we draw about the behavior of the near-horizon maximum? First, note that the maximum's angular elevation tends to increase with decreasing solar elevation and increasing optical depth. For example, in Fig. 6 the Sun is well above the horizon ($\theta_0 = 63°$), the atmosphere is very clear ($\tau_{aer} = 0.035$), and the maximum occurs at 2.1°

elevation. Conversely, in Fig. 9 the Sun has nearly set ($\theta_0 = 86°$) and, although visibility is still good ($\tau_{aer} = 0.0725$), the radiance maximum's elevation has increased to 8.3°. Second, the maximum's angular breadth increases with increasing optical depth. In Fig. 11 we have combined the measured radiance profiles from Figs. 6, 8, and 10. In order of increasing aerosol normal optical depth are the Bald Eagle Mountain sky of 5 February 1987 ($\tau_{aer} = 0.035$, Plate 38), the University Park sky of 6 October 1992 ($\tau_{aer} = 0.0925$, Plate 37), and the Bermuda sky ($\tau_{aer} = 0.245$, Plate 40). We can easily see in Fig. 11 that as aerosol loading increases, the radiance maximum broadens and becomes more poorly defined.

Using the Near-Horizon Maximum as a Quantitative Remote-Sensing Tool

Clearly the near-horizon radiance maximum depends on many variables, including solar elevation, atmospheric and surface absorptivity, and aerosol and
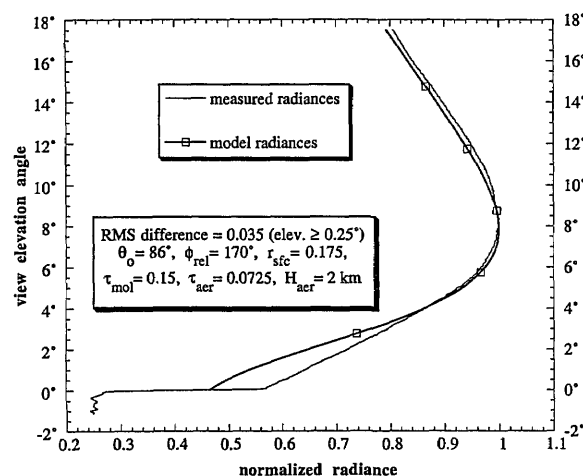

Fig. 9. Comparison of measured and modeled radiances for a clear-sky scene on the Chesapeake Bay (North Beach, Md.) at 2300 GMT on 24 March 1992 (see Plate 41, Ref. 24).
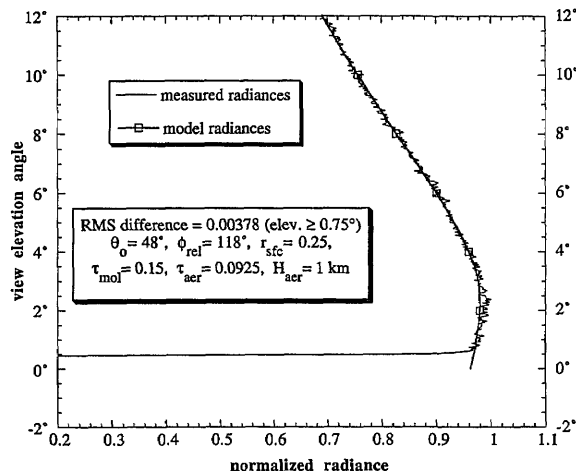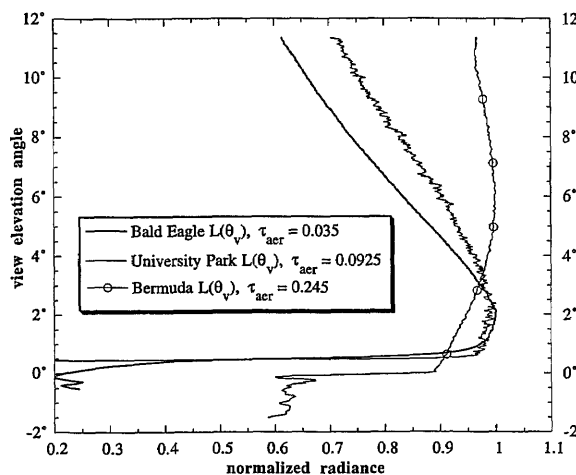

Fig. 11. Comparison of measured clear-sky radiance profiles in atmospheres with different aerosol normal optical depths τ_{aer}. See Plate 37 (University Park), Plate 38 (Bald Eagle), and Plate 40 (Bermuda) for the original photographs.

molecular scale heights and normal optical depths. Can any useful, observable patterns be made to emerge from this welter of details? The answer is yes, provided that we constrain some of our variables. For example, Fig. 12 is a nomogram from the second-order model that shows the maximum's angular elevation as a function of aerosol normal optical depth (or turbidity) and solar elevation. (Here we use the turbidity definition given by McCartney,[22] p. 206.) The nomogram is strictly valid only for fixed values of ϕ_{rel}, H_{aer}, and r_{sfc}, although in practice the latter two parameters have a much smaller effect on the diagram's details than does the relative azimuth. In Fig. 12, as elsewhere, the molecular normal optical depth $\tau_{mol} = 0.15$ and the single-scattering albedo $\varpi_0 = 0.97$.

Figure 12 reiterates some points made above, including the fact that the near-horizon maximum consistently rises with increasing optical depth. The maximum also *tends* to rise with decreasing solar elevation. To illustrate this trend, trace along a fixed optical depth from high to low Sun elevations. Note, however, that at large aerosol optical depths (say, $\tau_{aer} = 0.3$), the maximum will set slightly as the Sun moves downward from very high elevations.

Aside from illustrating the behavior of the second-order model, Fig. 12 serves as a practical observing tool: we can estimate aerosol optical depth based on the near-horizon maximum's elevation. For example, if you see a radiance maximum 3° above the antisolar horizon when the Sun's elevation is 21°, the normal aerosol optical depth is ~0.05 (turbidity ~1.33). Naturally such observations can be made with a radiometer as well as with the naked eye.

However, before seizing on Fig. 12 as a panacea for measuring turbidity, an important caveat needs to be considered. The near-horizon maximum often is visually subtle both because of its low contrast and

because its color and brightness changes are commingled (see Plate 38). Not surprisingly, the maximum's contrast is lowest when the optical depth is largest and multiple scattering is most pronounced (see, for example, Plate 40). Thus, although the maximum might exist at, say, 15° elevation, it may be so broad and of such low contrast that a naked-eye observer cannot see it or may misidentify its position. Nevertheless, if used judiciously, Fig. 12 gives us a way of turning a mere visual curiosity into a practical remote-sensing tool.

Conclusions

One of our goals is a simple physical explanation of the near-horizon radiance maximum. Figures 13 and 14 take two different tacks in attempting such an explanation. In Fig. 13, model radiances for several viewing directions near the horizon are plotted versus slant optical path length as measured from the observer. In other words, at each τ_{slant} along Fig. 13's ordinate, the three curves tell us what clear-sky radiances we would receive from each direction θ_v if the atmosphere's total optical depth were limited to the particular τ_{slant}. Obviously in the real atmosphere τ_{slant} increases with θ_v, so for each θ_v in Fig. 13 we have labeled the slant optical paths $\tau_f(\theta_v)$ over the entire atmosphere and their corresponding clear-sky radiances $L_f(\theta_v)$.

Notice what happens in Fig. 13 if we limit the total optical depth of the atmosphere [i.e., if we examine $L(\theta_v)$ at $\tau_{slant} < \tau_f$]. For very shallow atmospheres (say, $\tau_{slant} < 1.6$ for $\theta_v = 87°-90°$), radiance increases monotonically as we approach the horizon ($\theta_v = 90°$). For larger and more realistic values of the total slant optical path ($\tau_{slant} > 3.6$), the integrated clear-sky radiance $L(\theta_v)$ is largest at intermediate elevation angles ($\theta_v = 88.5°$).

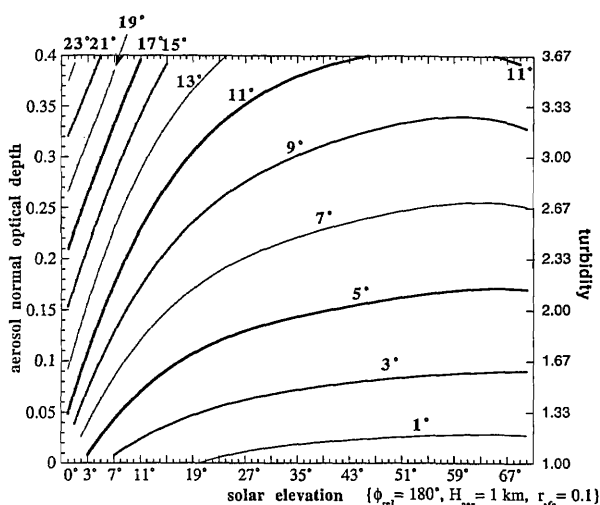Why do we see this change from the shallower atmosphere? As we thicken the atmosphere, in-

Fig. 12. Contours of the clear-sky radiance maximum's elevation as a function of solar elevation and aerosol normal optical depth. The observer is looking opposite the Sun ($\phi_{rel} = 180°$), the surface Lambertian reflectance $r_{sfc} = 0.1$, and the aerosol scale height $H_{aer} = 1$ km.
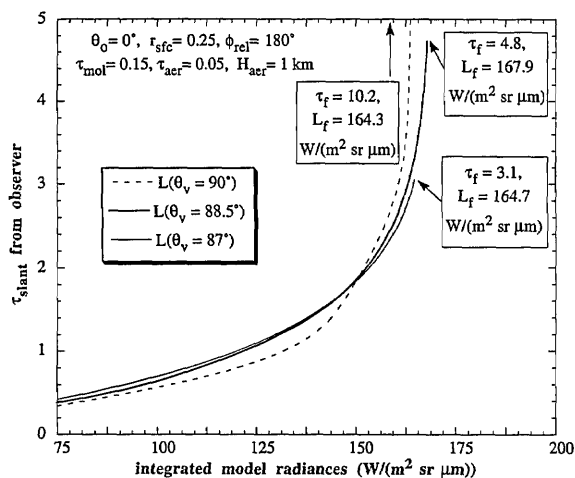
Fig. 13. Second-order model radiances integrated over slant optical path τ_{slant} at several view zenith angles θ_v. The total optical path lengths $\tau_f(\theta_v)$ are measured from the observer to the atmosphere's top and are paired with the corresponding clear-sky radiances $L_f(\theta_v)$.
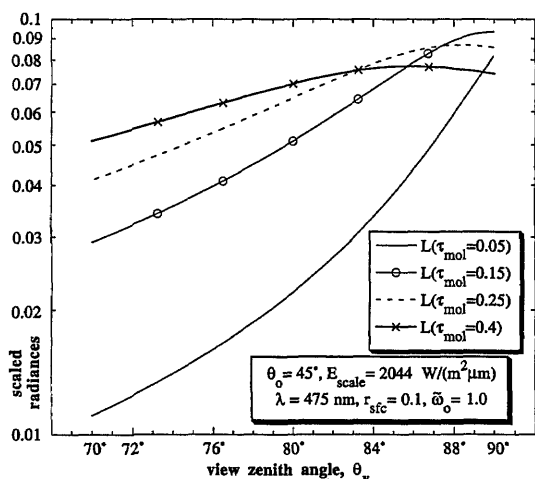
Fig. 14. Second-order model's meridional radiance profiles at $\phi_{rel} = 180°$ in a nonabsorbing, purely molecular atmosphere with different normal optical depths. In this atmosphere, the near-horizon radiance maximum does not exist for the two smaller optical depths, but it does for the two larger ones.

creased scattering of solar radiance L_s reduces the direct-beam source function J_{dir} at all altitudes. These reductions in J_{dir} are accompanied by corresponding increases in the multiple-scattering source function J_{diff}. However, if we make τ_{slant} large enough, at low altitudes the reductions in J_{dir} predominate over the cumulative increases in J_{diff}. The net result is that the total source function $J(\Psi, \tau)$ begins to decrease as we look along atmospheric paths very near the horizon (i.e., along paths dominated by low-altitude scattering). All other factors being equal, the τ_{slant} contribution to the local maximum will be most pronounced at the antisolar azimuth because τ_{slant} is largest for J_{dir} there. Of course, the scattering phase functions $P(\Psi)$ and surface reflectance r_{sfc} also affect the azimuthal behavior of the meridional radiance profiles.

Figure 14 offers further evidence of the role that optical depth plays in creating the near-horizon radiance maximum. As does Fig. 4, Fig. 14 shows us meridional radiance profiles from the second-order model, this time for a nonabsorbing, purely molecular atmosphere. (These curves have *not* been normalized by their respective maxima; multiplying each by E_{scale} yields absolute radiances.) Now, however, rather than keeping the atmosphere fixed and varying ϕ_{rel}, we fix ϕ_{rel} at 180° and vary the normal optical thickness of a purely molecular atmosphere. When the atmosphere is thin ($\tau_{mol} = 0.05$), radiances do indeed increase monotonically from zenith to horizon. Trebling optical depth to 0.15 still does not produce a local radiance maximum, although radiances increase very slowly within 2° of the horizon. However, if we increase τ_{mol} to 0.25 or 0.4, distinct local maxima appear at 1.75° and 4.5° elevation, respectively. Note too that as τ_{mol} increases, multiple scattering makes the zenith progressively brighter, ultimately at the expense of the horizon's brightness.

Restricting ourselves to a molecular atmosphere emphasizes the fact that the near-horizon radiance maximum does not require a highly anisotropic scattering medium. Although aerosols are not a prerequisite for the maximum's existence, they will usually change its details. For example, even in a slightly hazy atmosphere, a broad, intense solar aureole will dominate the horizon sky in the vicinity of a low sun. Because $\varpi_0 = 1.0$ in Figure 14, the graph also indicates that atmospheric absorption is not needed to produce the near-horizon radiance maximum. Although highly absorbing aerosols will darken the horizon sky (and the zenith), we do not need to invoke them to account for what we see.

Why does the clear daytime sky often have a near-horizon radiance maximum? A preliminary answer is that our atmosphere is just right: it absorbs very little in the visible, and its optical path length increases monotonically with decreasing view elevation angle (thus increasing total scattering along our line of sight). At the time, attenuation of direct sunlight reduces the source function $J(\Psi, \tau)$ when we look very near the horizon. For many combinations of normal optical depth and sun position, a subtle, yet discernible, brightness maximum results just above the horizon.

References and Notes

1. We use *radiance* and *brightness* as synonyms in this paper, while recognizing that they are not linearly related. For example, see G. Wyszecki and W. S. Stiles, *Color Science: Concepts and Methods, Quantitative Data and Formulae* (Wiley, New York, 1982), pp. 259 and 495.

2. R. Perez, J. Michalsky, and R. Seals, "Modeling sky luminance angular distribution for real sky conditions: experimental evaluation of existing algorithms," J. Illum. Eng. Soc. **21**, 84–92 (1992).

3. F. M. F. Siala, M. A. Rosen, and F. C. Hooper, "Models for the directional distribution of the diffuse sky radiance," J. Sol. Energy Eng. **112**, 102–109 (1990).

4. C. R. Prasad, A. K. Inamdar, and P. Venkatesh, "Computation of diffuse solar radiation," Sol. Energy **39**, 521–532 (1987).

5. J. V. Dave, "A direct solution of the spherical harmonics approximation to the radiative transfer equation for an arbitrary solar elevation. Part I: theory," J. Atmos. Sci. **32**, 790–798 (1975).

6. For basic discussions of optical path length's effect on sky radiance (in a purely molecular atmosphere) see C. F. Bohren and A. B. Fraser, "Colors of the sky," Phys. Teach. **23**, 267–272 (1985) and Ref. 7.

7. C. F. Bohren, "Multiple scattering of light and some of its

observable consequences," Am. J. Phys. **55,** 524–533 (1987).

8. G. Zibordi and K. J. Voss, "Geometrical and spectral distribution of sky radiance: comparison between simulations and field measurements," Remote Sensing Environ. **27,** 343–358 (1989).

9. R. L. Lee, Jr., "What are 'all the colors of the rainbow'?" Appl. Opt. **30,** 3401–3407, 3545 (1991).

10. D. K. Lynch and P. Schwartz, "Intensity profile of the 22° halo," J. Opt. Soc. Am. A **2,** 584–589 (1985).

11. A. Deepak and R. R. Adams, "Photography and photographic-photometry of the solar aureole," Appl. Opt. **22,** 1646–1654 (1983).

12. L. J. B. McArthur and J. E. Hay, "A technique for mapping the distribution of diffuse solar radiation over the sky hemisphere," J. Appl. Meteorol. **20,** 421–429 (1981).

13. M. A. Rosen, "The angular distribution of diffuse sky radiance: an assessment of the effects of haze," J. Sol. Energy Eng. **113,** 200–205 (1991).

14. A. W. Harrison, "Directional sky luminance versus cloud cover and solar position," Sol. Energy **46,** 13–19 (1991).

15. F. C. Hooper, A. P. Brunger, and C. S. Chan, "A clear sky model of diffuse sky radiance," J. Sol. Energy Eng. **109,** 9–14 (1987).

16. C. G. Justus and M. V. Paris, "A model for solar spectral irradiance and radiance at the bottom and top of a cloudless atmosphere," J. Cli. Appl. Meteorol. **24,** 193–205 (1985).

17. J. V. Dave, "Extensive datasets of the diffuse radiation in realistic atmospheric models with aerosols and common absorbing gases," Sol. Energy **21,** 361–369 (1978).

18. R. L. Lee, Jr., "Colorimetric calibration of a video digitizing system: algorithm and applications," Col. Res. Appl. **13,** 180–186 (1988).

19. A Photo Research PR-704 spectroradiometer with a nominal 0.5° FOV was used.

20. D. K. Lynch, "Step brightness changes of distant mountain ridges and their perception," Appl. Opt. **30,** 3508–3513 (1991).

21. C. F. Bohren and A. B. Fraser, "At what altitude does the horizon cease to be visible?" Am. J. Phys. **54,** 222–227 (1986).

22. E. J. McCartney, *Optics of the Atmosphere: Scattering by Molecules and Particles* (Wiley, New York, 1976), pp. 136–138.

23. As in the other models' simulations, all our radiance profiles are monochromatic. The wavelength λ used here is 475 nm, a typical dominant wavelength for the clear sky. This wavelength determines both the solar spectral irradiance and the angular scattering phase function for aerosols.

24. R. L. Lee, Jr., "Twilight and daytime colors of the clear sky," Appl. Opt. **33,** 4629–4638 (1994).

25. G. E. Shaw, "Sun photometry," Bull. Am. Meteorol. Soc. **64,** 4–10 (1983).